The Structural and Catalytic Properties of Isolated Pt²⁺ Sites in Platinum Phosphide (PtP₂)

Jiajing Kou, ^{a,b} Johnny Zhu Chen, ^b Junxian Gao, ^b Xiaoben Zhang, ^c Jie Zhu, ^d Arnab Ghosh, ^e Wei Liu, ^c A. Jeremy Kropf, ^f Dmitry Zemlyanov, ^g Rui Ma, ^h Xinwen Guo, ^d Abhaya K. Datye, ^e Guanghui Zhang, ^{*d} Liejin Guo, ^{*a} Jeffrey T. Miller*^b

KEYWORDS: isolated Pt²⁺ catalytic site, PtP₂ nanoparticle, propane dehydrogenation, *in situ* X-ray absorption spectroscopy, *in situ* resonant inelastic X-ray scattering

Corresponding Authors: <u>lj-guo@mail.xjtu.edu.cn</u> (LG), <u>gzhang@dlut.edu.cn</u> (GZ) and <u>mill1194@purdue.edu</u> (JTM)

^a State Key Laboratory of Multiphase Flow in Power Engineering, Xi'an Jiaotong University, 28 Xianning West Road, Xi'an, Shaanxi 710049, China

^b Davidson School of Chemical Engineering, Purdue University, 480 Stadium Mall Drive, West Lafayette, IN 47907, United States

^c Dalian National Laboratory for Clean Energy, Dalian Institute of Chemical Physics, Chinese Academy of Sciences, Dalian, Liaoning 116023, China

^d State Key Laboratory of Fine Chemicals, PSU-DUT Joint Center for Energy Research, School of Chemical Engineering, Dalian University of Technology, Dalian, Liaoning 116024, China

^e Department of Chemical and Biological Engineering, University of New Mexico, Albuquerque, NM 87131 United States

^f Chemical Science and Engineering Division, Argonne National Laboratory,9700 South Cass Avenue, Lemont, IL 60439, United States

^g Birck Nanotechnology Center, Purdue University, 1205 W State St., West Lafayette, IN, 47907, United States

^h Chemistry and Chemical Engineering Guangdong Laboratory, Shantou 515031, China

ABSTRACT

This manuscript describes the synthesis and catalytic properties of supported, 2-3 nm PtP₂ nanoparticles (NPs). Depending on the P loading, two Pt phosphide structures are formed, i.e., a PtP₂ surface on (metallic) Pt core (Pt@PtP₂) and a single phase PtP₂ nanoparticle (NPs). The structures were determined by extended X-ray absorption fine structure (EXAFS), in situ synchrotron X-ray diffraction (sXRD) and scanning transmission electron microscopy (STEM). In PtP₂ NPs, Pt²⁺ ions are geometrically isolated by P₂²⁻ ions, and at a Pt-Pt distance of 4.02 Å, which is much longer than 2.78 Å in (metallic) Pt NPs. The oxidation state of Pt in PtP2 NPs was determined by in situ X-ray absorption near edge structure (XANES) and in situ X-ray photoelectron spectroscopy (XPS), and was consistent with Pt²⁺ ions even after treatment in H₂ at 550°C. Unlike Pt NP's which are highly active for propylene hydrogenation at room temperature, PtP₂ NPs are not active below about 150°C suggesting the absence of metallic surface Pt. In contrast to metallic Pt, which is poorly selective for acetylene hydrogenation, PtP₂ nanoparticles display a high selectivity towards ethylene. PtP₂, also, has high olefin selectivity for propane dehydrogenation; while the rate per g Pt is about 7 times lower than metallic Pt NPs of the same size. In situ resonant inelastic X-ray scattering (RIXS) spectroscopy shows that the energy of the filled Pt 5d valence orbitals is 1.5 eV lower than that of metallic Pt, which leads weaker adsorbate binding consistent with its catalytic properties. A H₂-stable Pt²⁺ site suggests different catalytic applications for these catalysts compared to Pt NPs.

1. INTRODUCTION

The majority of commercial process for production of petrochemicals and fuels utilize heterogeneous catalysts, and platinum is one of the most versatile active metals for many reactions. Pt is highly effective for both oxidation and reduction reactions and for the majority of these applications, metallic Pt is the active form of the catalyst. In addition, bimetallic alloys 1-10 are generally more selective and stable widely and have been studied hydrogenation/dehydrogenation^{3, 11}, naphtha reforming^{3, 12-13}, water gas shit reaction¹⁴⁻¹⁵, biomass reforming¹⁶, auto exhaust emission control, CO and hydrocarbon oxidation¹⁷⁻¹⁸, electro-catalytic transformation¹⁹⁻²¹, etc. For example, Pt-Sn bimetallic catalysts have been widely studied and used as industrial catalysts for propane dehydrogenation to propylene.²²⁻²³ The incorporated Sn atoms dilute large Pt ensembles, which effectively inhibits side reactions such as hydrogenolysis and coke formation. In addition, Sn modifies the energy of the Pt 5d orbitals, which weakens the metal-adsorbate bond energies. However, Pt-based bimetallic catalysts still suffer from coking and sintering, and require carbon burning and Cl₂ regenerative treatments, while phase segregation and separation occasionally occurs, causing irreversible deactivation of bimetallic catalysts.²⁴⁻²⁶ Because of their industrial and fundamental importance, the development of new catalytic materials with new properties and potentially new reactions remains an active research field.

Metal phosphides can usually be understood as P doped metal "alloys", and the bond formation of metal and P atoms can greatly modify the geometric and electronic structure of metal atoms, similar to bimetallic alloys. ²⁷⁻²⁹ However, compared with bimetallic alloys, the smaller size and higher electronegativity of P atom offers additional flexibility for obtaining desired properties, which provide a feasible strategy for robust catalyst design. 30-31 Metal-rich metal phosphides, for example, M₃P, M₂P and MP, with structures containing metal-metal bonds, display metallic properties for a number of heterogenous catalytic applications³² including electrochemistry³³ for hydrogen evolution³⁴⁻³⁵, hydroprocessing for removal of S, N and O from petroleum^{27, 36-40}, olefin hydroformylation⁴¹, alkane dehydrogenation⁴²⁻⁴⁴, etc. Transition metal phosphides often have high thermal stability, which suggests these might be potential catalysts for high temperature reactions. 43-46 For example, the Ni₂P has a higher olefin selectivity than Ni NP's for propane dehydrogenation at 550°C. The improved olefin selectivity was suggested to be due to weaker olefin adsorption and better coke resistance. 43-44 A more metal-rich phase, Ni₁₅P₂, however, led to increased deactivation. 44 Similar findings were found for Ru phosphide catalysts. RuP nanocrystal catalyst displayed high olefin selectivity and better stability for propane dehydrogenation than Ru₂P.⁴⁷ In contrast with Ni, Fe and Ru NPs, which convert alkanes to methane and coke with little selectivity to olefins, metal phosphides with the proper structure can have the high activity of the Group 8 metal NPs but with the high catalytic selectivity and improved stability. The thermal stability and excellent catalytic performance of Ni₂P and RuP compared to the pure metal NPs suggest that Pt phosphide might also be an effective hydrogenation/dehydrogenation catalyst.

In this work, we report a series of supported, 2-3 nm Pt phosphide (PtP₂) catalysts with non-metallic character. The Pt phosphide catalyst structures were determined by *in situ* XAS, *in situ* synchrotron X-ray diffraction (sXRD), and scanning transmission electron microscopy (STEM). The oxidation state of Pt in the Pt phosphide catalysts was determined to be Pt²⁺ by XANES and X-ray photoelectron spectroscopy (XPS). Thus, the catalytic site in PtP₂ NPs is an isolated Pt²⁺ ion

on the NP surface. *In situ* resonant inelastic X-ray scattering (RIXS) was used determine the effect of P₂²⁻ ions on the energy of the Pt 5d valence orbitals compared to monometallic Pt NPs. The structural and electronic changes provide fundamental understanding of the role of P on the catalytic performance. Propane dehydrogenation, propylene hydrogenation and acetylene selective hydrogenation were performed to evaluate the catalytic properties. Unlike metallic Pt NPs, PtP₂ does not chemisorb CO, nor hydrogenate olefins at room temperature. PtP₂ catalysts display high olefin selectivity for propane dehydrogenation with rates approaching that of metallic Pt NPs and significantly higher than other non-metallic, single site dehydrogenation catalysts. PtP₂ shows significantly higher ethylene selectivity for acetylene hydrogenation than Pt NPs. These results demonstrate that the different catalytic properties of isolated Pt²⁺ catalytic sites have potential for better performance than Pt NPs for some reactions, especially those where single site ions are the preferred active site.

2. EXPERIMENTAL SECTION

2.1. Catalyst Synthesis.

All catalysts were synthesized by sequential incipient wetness impregnation (IWI). To prepare Pt/SiO₂ with target Pt loading of 2 wt%, 0.2 g of tetraamine platinum nitrate [Pt(NH₃)₄(NO₃)₂, 99.995%] was dissolved in 2.75 mL de-ionized (DI) water, and concentrated NH₄OH was added to obtain a clear solution with pH around 11. This solution was added dropwise to 5.0 g silica gel (SiO₂, 480 m²/g, 0.75 mL/g pore volume, 99%) with continuous stirring. The obtained sample was dried at room temperature (RT) for 3 h before drying at 105°C overnight, and then calcined at 225°C for 3 h. The reduction step of Pt/SiO₂ was performed under 5% H₂/N₂ at 225°C for 30 min, and then 250°C for 30 min, followed by 550°C for another 30 min.

To prepare Pt-P catalysts, the Pt/SiO₂ was first obtained by the above method but not reduced. The amount of phosphoric acid [H₃PO₄, 85% aq.] based on the P/Pt molar ratio of 10:1,20:1 and 50:1, was dropwise added to the unreduced Pt/SiO₂. The obtained solid was dried at RT for 3 h before drying in the oven at 105°C overnight, and then calcined at 600°C for 1 h. The Pt-P samples were finally reduced at 550°C under 5% H₂/N₂. The obtained catalyst was denoted as Pt-P-*x*, where *x* denotes as the molar ratio of P/Pt. Pt-P-10, Pt-P-20 and Pt-P-50 were synthesized by this method, respectively. For comparison, a P/SiO₂ sample were prepared using the same method and with the same P loading as that of the Pt-P-50 sample.

2.2. Characterizations.

Scanning Transmission Electron Microscopy (STEM). The atomic resolution microscopy analysis for Pt-P catalysts was performed on a JEM ARM200F thermal-field emission microscope with a probe Cs-corrector working at 200 kV which is located at electron microscopy center of Dalian Institute of Chemical Physics (DICP), Chinese Academy of Sciences. For the high angle annular dark-field (HAADF) imaging, the convergence angle of ~23 mrad and collection angle range of 68~174 mrad were adapted for the incoherent atomic number imaging.

Additionally, the Titan Themis G3 environmental transmission electron microscope (ETEM, Thermo Scientific Company) operated at 300 kV in TEM mode was utilized as complementary to ARM200F microscopy for imaging the Pt-P-50 catalyst. For all the STEM/TEM sample preparation, catalysts were dispersed in ethanol and dropped onto copper grids and dried on a hot plate (150°C). Several images were taken from randomly selected locations on the catalysts to perform size distribution based on over 400 nanoparticles.

In Situ X-ray Absorption Spectroscopy (XAS). In situ XAS measurements at the Pt L₃ edge (11.564 keV) in transmission mode were performed at the 10-BM-B beamline at the Advanced Photon Source (APS), Argonne National Laboratory. Catalysts and reference compounds were ground into fine powders and pressed into a sample holder containing six wells. Then the holder was loaded into a quartz tube allowing gas flow so that samples could be treated prior to measurements. The catalysts were treated with 3.5% H₂/He at 550°C, then cooled to RT in flowing He before moving to the beamline to acquire data. For internal energy calibration, a Pt foil scan was simultaneously obtained. Athena software was used to calibrate energy and normalize the data, and the edge energy was determined by the first maximum peak in the first derivative of X-ray absorption near edge structure (XANES) spectra. 48 EXAFS spectra were fit using a least-squared fit in R-space of k²-weighted Fourier transform (FT) to determine coordination number (CN) and bond distances (R) between Pt and its neighbors using the Artemis software ⁴⁸, and the k range for Fourier transform of Pt L₃ edge was $\Delta k = 3.0 \sim 12.0 \text{ Å}^{-1}$. The S₀² value was determined from fitting the Pt foil standard. The $\Delta \sigma^2$ values were initially determined from the k² weighted EXAFS of the inverse Fourier transform of the isolated first shell in k-space for each catalyst, and all samples were similar. However, in order to determine trends due to small changes in structure, fits were done holding $\Delta \sigma^2$ constant at the average value.

X-ray Photoelectron Spectroscopy (XPS). XPS measurement was performed using a Kratos AXIS Ultra DLD Imaging spectrometer, using monochromatic Al Kα radiation as an excitation source. Prior to spectra acquisition, fresh catalysts were reduced in a catalyst cell by 5% H₂ balanced with Ar at 550°C for 1 h, and then transferred under ultra-high vacuum (UHV) into the analysis chamber without exposure to air. The data was analyzed with CasaXPS software. For charge correction, the C 1s peak of the adventitious carbon was set to a binding energy of 284.8 eV. The background was subtracted using Shirley line shape, and curve-fitting was performed using synthetic function of Lorentzian blended with Gaussian.

In Situ Synchrotron X-ray Diffraction (sXRD). In situ sXRD measurements were performed at the 11-ID-C beamline at the APS, Argonne National Laboratory. The data were collected in transmission mode by a PerkinElmer large-area detector using X-rays of λ=0.1173 Å at 105.091 keV calibrated by fitting the diffraction pattern of the CeO₂ reference. Samples were pressed into thin wafers, then loaded into a Linkam Scientific TS1500 heating stage equipped with water cooling. Prior to measurements the stage was purged with He for 5 min at RT and then ramped to 550°C in 3.5% H₂/He at 50 mL/min. Diffraction patterns were acquired after reduction at 550°C for 20 min, and also collected at 35°C after being cooled down in the same atmosphere. The 2-D scattering images were integrated to 1-D intensity versus 2θ plots by using Fit2D software. Materials Analysis Using Diffraction (MAUD) software was used to simulate standard diffraction patterns of Pt FCC and PtP₂ phases which were used to determine the crystal structure of Pt-P catalysts in comparison with experimental diffraction patterns. ⁵⁰

In Situ Resonant Inelastic X-ray Scattering (RIXS). RIXS measurements were performed at the MR-CAT 10-ID beamline at the APS, Argonne National Lab. Samples were pressed into self-supporting wafers and were measured at 45° angle with respect to the incident beam. The small reactor with internal resistively-heated plates has been previously described.⁵¹ Samples were reduced at 550°C in 3% H₂/He at 50 mL/min for 20 min and then cooled to 200°C for measurement.

A spectrometer based on the Laue geometry was used for RIXS measurements and has been described previously.⁵ The cylindrically-bent silicon analyzer crystal had the following properties: $\rho = 350$ mm, thickness 55 μ m, [100] wafer normal, <133> reflection. The entire emission spectrum was collected at each incident energy; both the analyzer and detector positions were fixed during measurements.

In Situ Infrared Spectroscopy (IR). In situ diffuse reflectance infrared Fourier transform (DRIFT) spectra were collected on a Nicolet iS50 spectrometer with a mercury cadmium telluride (MCT) detector cooled by liquid nitrogen. Prior to the test, ~20 mg of the sample was reduced at 550°C under 5% H₂ for 30 min, and the background spectrum was collected after purging with N₂ at room temperature for 40 min. Then the pre-reduced samples were exposed to 10 vol.% CO in N₂ at 25°C for 40 min, and the sample IR spectra were collected after purging with N₂ for 40 min.

2.3. Catalytic Evaluation.

Propylene Hydrogenation and Propane Dehydrogenation. Propylene hydrogenation and propane dehydrogenation were carried out in a quartz fixed-bed reactor with a quartz tube of 3/8 in. OD. To vary the initial conversion, the loaded catalysts ranging from 10 to 300 mg were diluted with SiO₂ to 1.0 g. A thermocouple was placed at the center of the catalyst bed to measure the reaction temperature. Before each test, the catalyst was reduced for 30 min at 550° C with 100 mL/min 5% H₂/N₂. The flow of 5% C₃H₈ and 5% H₂ were adjusted to vary the initial conversion for PDH at a reaction temperature of 550° C. The gas products were analyzed with an Agilent 7890A gas chromatograph system equipped with a Flame Ionization Detector (FID). In PDH, five kinds of light hydrocarbons were detected: CH₄, C₂H₆, C₂H₄, C₃H₈ and C₃H₆. The propane conversion and propylene selectivity were calculated using Eq. (1) and (2). The rate of reaction was calculated using Eq. (3). A first-order deactivation model was used to estimate the rate of catalyst deactivation, and the deactivation coefficient (k_d) was determined as shown in Eq. (4) where $Conv_0$ is defined as the initial conversion and $Conv_t$ is the conversion at the time t.

Conversion (%) =
$$\frac{\text{moles of } C_3H_8 \text{ in inlet-moles of } C_3H_8 \text{ in outlet}}{\text{moles of } C_3H_8 \text{ in inlet}} \times 100\%$$
 (1)

Selectivity (%) =
$$\frac{\text{moles of } C_3 H_6}{\text{moles of } C_3 H_6 + \frac{2 \times \text{moles of } C_2}{3} + \frac{\text{moles of } CH_4}{3}} \times 100\%$$
 (2)

$$Rate = \frac{\text{molar flow rate of } C_3H_8 \times Conversion}{\text{moles of Pt}}$$
(3)

$$k_d = \frac{\ln\left(\frac{1 - Conv_t}{Conv_t}\right) - \ln\left(\frac{1 - Conv_0}{Conv_0}\right)}{t} \tag{4}$$

Acetylene Selective Hydrogenation. Selective hydrogenation of acetylene was carried out in a 6 mm OD quartz tube with glass wool plugs on each side to retain the catalyst. Pt/SiO₂ and Pd/Al₂O₃ catalysts were used as reference catalysts, with 20 mg of catalyst diluted with equal volume of SiC. Due to their lower reactivity, the Pt-P powders were tested with 180 mg of catalyst to achieve similar conversions of acetylene. A thermocouple was placed in the catalyst bed to

measure the reaction temperature. Before each test, each catalyst was reduced for 60 min at 350° C with 50 mL/min 4% H₂/N₂. The reactant gas was composed of 1% C₂H₂, 4% H₂ and rest balanced with N₂ at a total flow rate of 50 mL/min. The acetylene conversion and ethylene selectivity were calculated as shown below:

Acetylene Conversion (%) =
$$\frac{\text{moles of } C_2H_2 \text{ in inlet-mole of } C_2H_2 \text{ in outlet}}{\text{moles of } C_2H_2 \text{ in inlet}} \times 100\%$$
 (5)

Ethylene Selectivity (%) =
$$\frac{\text{moles of } C_2H_4 \text{ in outlet}}{\text{moles of } C_2H_2 \text{ in inlet-mole of } C_2H_2 \text{ in outlet}} \times 100\%$$
 (6)

3. RESULTS

3.1. Synthesis of Silica Supported Pt Phosphide Catalysts. Transition metal phosphides are most often synthesized as colloidal NPs using metal-organic precursor decomposition⁵², solvothermal⁵³, solid phase reaction⁵⁴ methods. Typically, the NP sizes are larger than 5 nm, and often much larger, which are not ideal for catalytic applications. In addition, the synthesis approaches are not easily reproduced for large scale applications. Here Pt phosphides are directly synthesized on a higher surface area oxide support. The synthesis approach is to first impregnate an aqueous solution of the Pt(NH₃)₄(NO₃)₂ onto the silica surface in NH₄OH. The basic solution deprotonates the support hydroxyl groups leading to a negative surface charge. Under these impregnation conditions the Pt(NH₃)₄²⁺ ions are uniformly distributed.⁵⁵ After drying, aqueous solutions of phosphoric acid are added, dried and heated in air to 600°C. Since these catalysts will be used for hydrogenation reactions, they were additionally reduced at 550°C. At these high temperatures the metal salts reduce to form Pt phosphide. P to Pt molar ratios were prepared from 1 to 50. For P to Pt ratios below about 4, the NPs were largely metallic Pt; while at ratios greater than about 10, predominantly PtP₂ was formed.

The particle sizes of these Pt-P catalysts as well as Pt/SiO₂ were determined by STEM. The uniform distribution of the bright spots suggests a narrow range of the particle sizes shown in **Figure 1**. The particle size distributions of all catalysts are similar ranging between 2-3 nm. For example, the average particle size of Pt/SiO₂ is 2.1 nm, and the average particle sizes of Pt-P-10, Pt-P-20 and Pt-P-50 are 2.7, 2.6 and 2.4 nm, respectively.

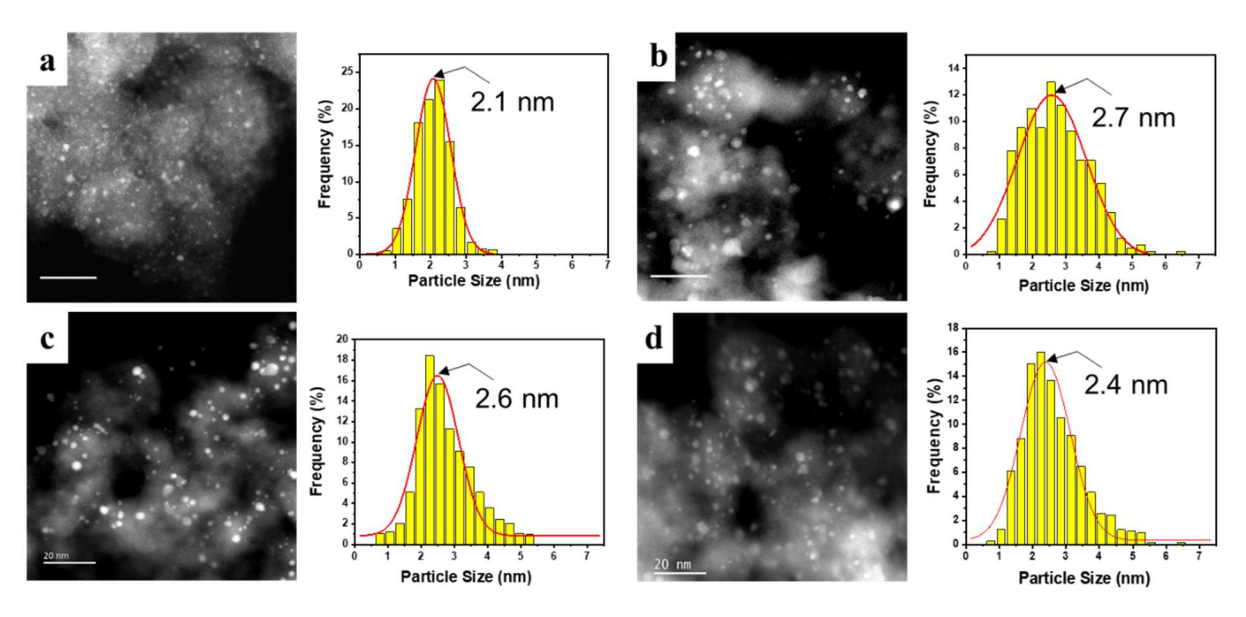


Figure 1. STEM images and particle size distributions for (a) Pt/SiO₂, (b)Pt-P-10, (c) Pt-P-20, (d)Pt-P-50.

3.2. Geometric Structures of Pt and Pt-P Nanoparticles. The local Pt coordination was determined by XAS at the Pt L₃ edge (11.564 keV). **Figure 2** shows the k²-weighted magnitudes of the FT of EXAFS spectra of Pt and Pt-P NPs. The magnitude and imaginary parts of the FT of the EXAFS at Pt L₃ edge of all catalysts were fitted to determine the coordination number (CN) and bond distances (R), as shown in **Figure S1** and **Table 1**. The spectrum of Pt/SiO₂ shows the same shape and peak position as a Pt foil (**Figure 2**a), where there are three main peaks between about 2 Å and 3 Å (phase uncorrected distance), indicating these samples were fully reduced. The Pt-Pt coordination number (CN_{Pt-Pt}) of Pt/SiO₂ was 8.1 at 2.74 Å, and the lower CN_{Pt-Pt} and slightly shorter bond distance (2.74 Å) compared to those of the Pt foil (2.77 Å) are typical of nanoparticles. ⁵⁶

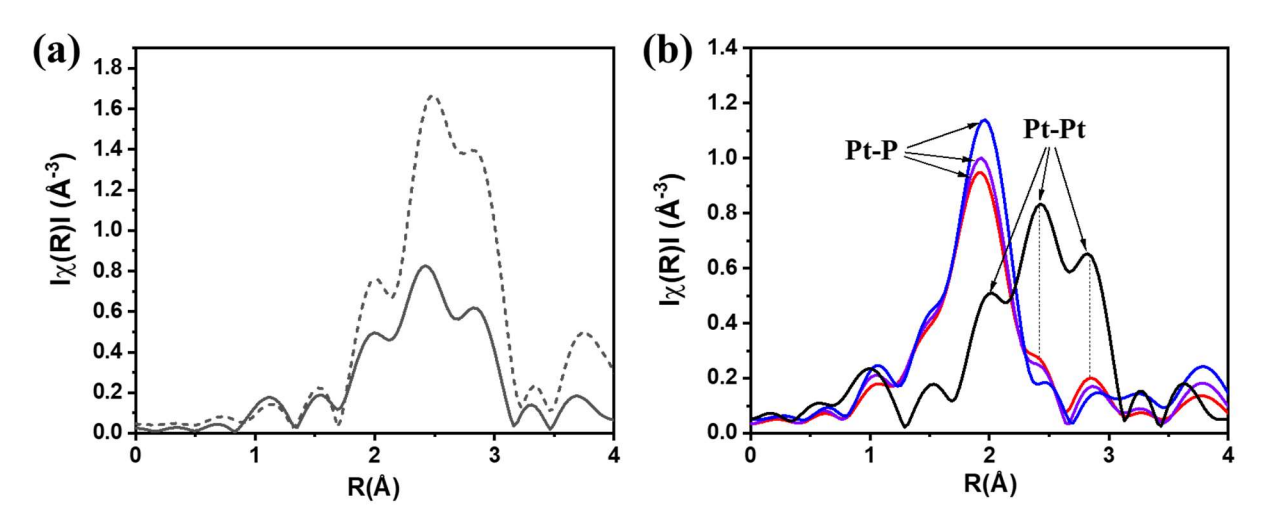


Figure 2. The k²-weighted magnitudes of the FT of EXAFS spectra at the Pt L₃ edge of (a) Pt foil (dash line) and Pt/SiO₂ (black line), (b) Pt/SiO₂ (black line), Pt-P-10 (red line), Pt-P-20 (purple line) and Pt-P-50 (blue line).

Table 1. Edge Energy and EXAFS Data at the Pt L₃ Edge for the Fully Reduced Supported Pt Catalysts

Catalyst	Edge energy (keV)	Scattering path	R(Å)	CN	σ^2
Pt/SiO ₂	11.5640	Pt-Pt	2.74 ± 0.02	8.4 ± 0.8	0.007 ± 0.001
Pt-P-10	11.5652	Pt-Pt	2.76 ± 0.01	2.4 ± 0.4	0.007 ± 0.001
		Pt-P	2.33 ± 0.02	3.5 ± 0.2	0.007 ± 0.001
Pt-P-20	11.5654	Pt-Pt	2.76 ± 0.01	1.8 ± 0.4	0.007 ± 0.001
		Pt-P	2.34 ± 0.01	3.7 ± 0.5	0.007 ± 0.001
Pt-P-50	11.5655	Pt-P	2.36 ± 0.01	4.4 ± 0.4	0.007 ± 0.001

For comparison, the k²-weighted magnitudes of the FT of EXAFS spectra of Pt and Pt-P NPs were shown in **Figure 2b**. The Pt-P-50 catalyst has a very different spectrum from Pt NPs (blue spectrum). A large peak located around 2 Å indicates the presence of shorter bonds, but no peaks were observed in the region where Pt-Pt scattering is expected. The spectrum was fitted with a Pt-P scattering, where the Pt-P coordination number (CN_{Pt-P}) of 4.4 at 2.36 Å was obtained.

Compared with Pt-P-50 and Pt NPs, the EXAFS spectra of Pt-P-10 and Pt-P-20 catalysts show a large peak at about 2 Å and much smaller peaks between 2-3 Å, suggesting the presence of Pt-P bonds and small fraction of Pt-Pt bonds, respectively, as shown in **Figure 2**b and **Figure S2**. Thus, two scattering pairs of Pt-Pt and Pt-P were used to fit the EXAFS of Pt-P-10 (**Figure S1**), resulting

in a CN_{Pt-Pt} of 2.4 at 2.76 Å and CN_{Pt-P} of 3.5 at 2.33 Å. The Pt-Pt bond distance of 2.76 Å is characteristic of metallic Pt. The small coordination number in these two samples suggests only minor amounts of metallic Pt. As the P loading increases, e.g. Pt-P-20, the CN_{Pt-Pt} decreases slightly to 1.8 at 2.76 Å and the CN_{Pt-P} increases to 3.7 at 2.33 Å.

While XAS shows there are Pt-P bonds in these catalysts, X-ray absorption is a local scattering technique and does not provide information on the crystalline order of the NPs. Because of their small size, *in situ* synchrotron diffraction (sXRD) was required to identify the phase. Due to the high X-ray energy (105.70 keV or λ =0.1173 Å), the resulting diffraction patterns were obtained at lower 20 angles than those from a laboratory difractometer, typically from 0 to 10°, as shown in **Figure 3.** The high flux of the synchrotron x-ray beam also gives a better signal-to-noise ratio to characterize the NPs. In order to reduce the effects of thermal strain, the sXRD patterns for all the catalysts were obtained at room temperature in H₂ atmosphere after reduction in H₂ at 550 °C. **Figure 3** shows the reflections of Pt-P-10 match those of simulated Pt face centered cubic (FCC) structure. Although XAS suggested two components in Pt-P-10, the sXRD pattern shows only metallic Pt NPs. It is likely that scattering from the small size and the weak scatting of the P atoms that the diffraction pattern of the Pt phosphide regions could not be detected. For Pt-P-20, in addition to the characteristic peaks of Pt FCC, there are additional peaks in the sXRD which match PtP₂ (ICSD 9015002). For Pt-P-50, there were large peaks due to the P species that dominated the diffraction pattern, thus the structure of the Pt-P phase could not be determined.

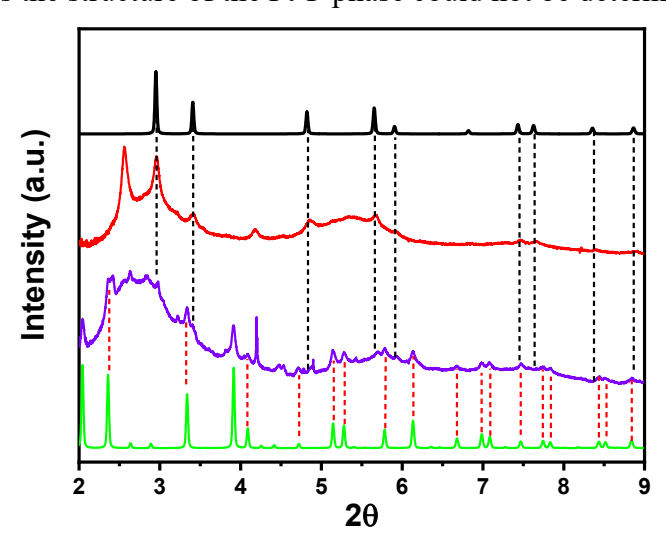


Figure 3. Synchrotron XRD patterns of Pt-P-10 (red line), Pt-P-20 (purple line), Pt simulation (black line, ICSD 9012957) and PtP₂ simulation (green line, ICSD 9015002).

To confirm the structure of Pt-P-50 catalyst, high angle annular dark field (HAADF) STEM was conducted on Pt-P-50, and image is shown in **Figure 4**. The atomic resolution STEM shows a highly ordered NP with a zone axis<001> for Pt-P-50. The lattice spacing of 2.81 Å is ascribed to (020) and (200) planes of the PtP₂ structure. The image contrast confirms that the Pt-P-50 shows a fully ordered PtP₂ structure in agreement with the EXAFS results.

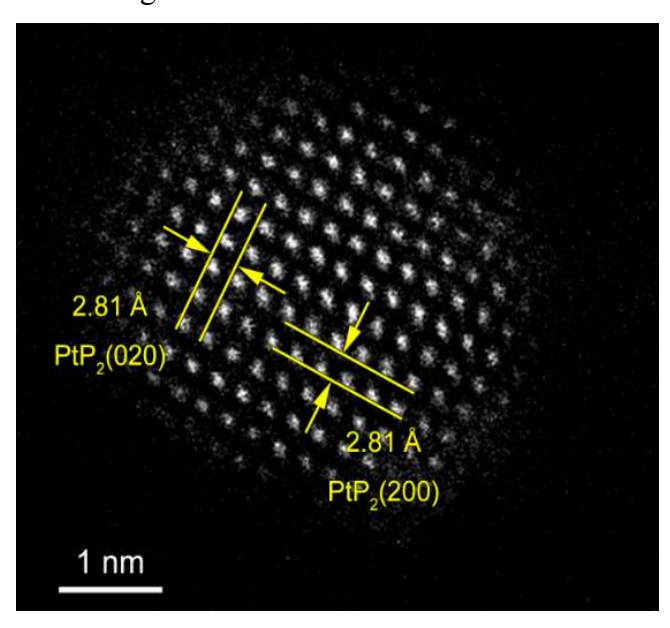


Figure 4. High-resolution STEM image of Pt-P-50 catalyst.

In summary, the Pt-P-50 is a fully ordered PtP₂ structure confirmed by STEM and EXAFS; while, there are both Pt and PtP₂ domains within the NPs present in Pt-P-10 and Pt-P-20 as evident from EXAFS and XRD. To better understand the structures of the latter two catalysts, the surface composition of the NPs was determined by difference analysis of *in situ* XAS under reducing and mild oxidizing conditions.^{4, 6, 57} The k²-weighted magnitudes of the FT of EXAFS spectra of reduced and oxidized Pt-P catalysts are shown in **Figure 5**. There is no change in these spectra between reduced (solid) and oxidized (dotted) for either PtP₂ structure (**Figure 5**b) or the Pt-P-20 catalyst (**Figure 5**a) which contains both PtP₂ and Pt. Similar results were obtained for Pt-P-10 (**Figure S3**). The XANES spectra of the Pt-P-50, Pt-P-20 and Pt-P-10 (**Figure S4**) also showed no change upon oxidation consistent with the EXAFS results.

Metallic Pt is oxidized in air at room temperature leading to the loss of Pt-Pt bonds and the formation of Pt-O bonds. The absence Pt oxidation in Pt-P-10 and Pt-P-20 suggests that there is no metallic surface Pt but is likely PtP₂. Thus, the remaining Pt-Pt scattering observed by XAS and

sXRD is from the NP core. In other words, Pt-P-10 and Pt-P-20 appear to be core-shell structures with PtP₂ shell with a metallic Pt core. The core-shell structure is also confirmed by the catalytic performance which will be shown later. The absence of exposed metallic Pt is also confirmed by the DRIFT spectra of CO. Pt NPs readily absorb CO; while there are no DRIFTS peaks of Pt phosphide exposed to CO (**Figure S5**). The lack of reactivity with room temperature air and the inability to absorb CO suggests that the chemical reactivity of PtP₂ is very different from Pt NP's.

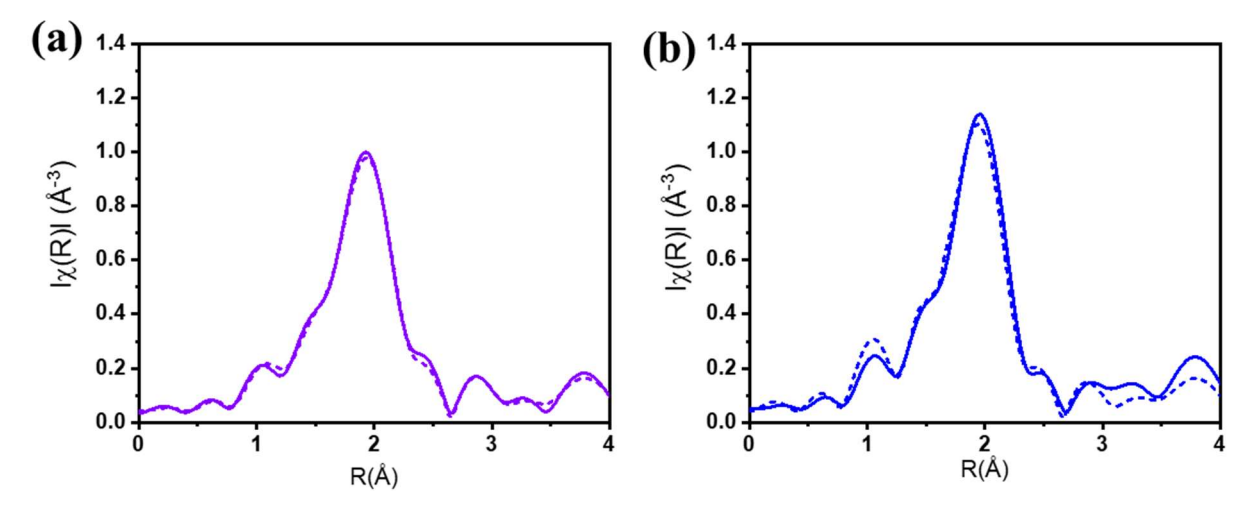


Figure 5. The k²-weighted magnitudes of the FT of EXAFS spectra for (a) reduced (purple solid line) and oxidized (purple dashed line) Pt-P-20 and (b) reduced (blue solid line) and oxidized (blue dashed line) Pt-P-50.

Figure 6 shows the XANES spectra of Pt-P samples together with Pt NPs. The XANES spectra of Pt/SiO₂ (black line) shows that the shape, white line intensity and edge energy are similar to that of Pt foil, as shown in **Figure S6**. The edge energy was determined from the inflection of the leading edge of the XANES spectrum for all samples, and is given in **Table 1**. For all Pt-P catalysts, the edge shifted to higher energies, and there is an increase in the intensity of the white line, i.e. the first peak beyond the edge. The white line intensity is associated with ionization of the 2p electron to the unfilled Pt 5d orbitals, and an increased intensity is consistent with fewer electrons in 5d orbitals, i.e. a higher oxidation state. As the amount of P in the catalysts increased, both the edge energy and white line intensity increased slightly (**Table 1**). The maximum XANES edge energy shift of 1.5 eV and maximum white line intensity were observed in Pt-P-50 catalyst (PtP₂ NPs). Since the Pt-P-20 and Pt-P-10 are core-shell structures, i.e, contain both metallic Pt and Pt phosphide, the edge energies were slightly lower than that of Pt-P-50.

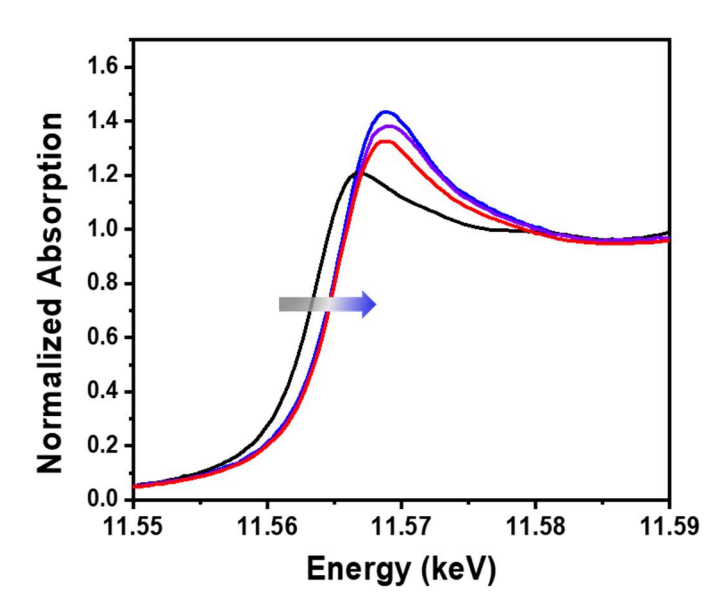


Figure 6. Normalized XANES spectra at the Pt L₃ edge of Pt/SiO₂ (black line), Pt-P-10 (red line), Pt-P-20 (purple line) and Pt-P-50 (blue line);

The XANES combination fitting for the Pt-P-20 and Pt-P-10 was done to estimate the compositions of Pt and PtP₂) as shown in **Figure S7** and **Table S1**. The Pt/SiO₂ and Pt-P-50 were used as the reference standards for the XANES fits. The fraction of metallic Pt is estimated at 25% and 15% for Pt-P-10 and Pt-P-20, respectively.

One can estimate the volume of the Pt core from the fraction of Pt atoms by XANES, the TEM size and size of the Pt unit cell. The Pt unit cell size is 0.392 nm, which give a cell volume of 0.06 nm³. The number of atoms in a NP of different sizes can be estimated by $4/3\pi R^3$. NP of 1, 1.5, 2 and 2.5 nm have about 9, 29, 70 and 136 atoms respectively. For NPs with about 20% of metallic atoms at the core, this would be about 27 atoms, or about 1.5 nm size. Thus, the shell is about 0.5 nm giving a 2.5 nm PtP₂ on Pt core. These estimates suggest a surface PtP₂ of about 2-3 atomic layers in the core-shell catalysts.

3.3. Chemical State of Pt in PtP2 Nanoparticles. *In situ* XPS was employed to determine the oxidation state of Pt in the Pt-P catalysts, **Figure 7**. The Pt 4f region consists of two components, which correspond to two spin-orbital splitting peaks of Pt $4f_{7/2}$ (at lower binding energy) and Pt $4f_{5/2}$ (at higher binding energy). As a reference, Pt/SiO₂ exhibits a Pt $4f_{7/2}$ peak at 71.8 eV, which is assigned to metallic Pt. This value is higher than the binding energy of Pt bulk metal at 71.0 eV, due to the decreased extra-atomic relaxation of small metal particles. For Pt-P-50, the Pt $4f_{7/2}$ binding energy is at 73.0 eV, 1.2 eV higher than that of Pt NP's, which can be attributed to Pt²⁺ in

the NPs consistent with the shift to higher energy in the XANES spectra. In addition, the binding energy of P 2p peak is 135.3 eV (**Figure S8**), indicating that the majority of P, which is present in large excess of that required to form PtP₂, is present as P⁵⁺, likely P₂O₅. ⁵⁹

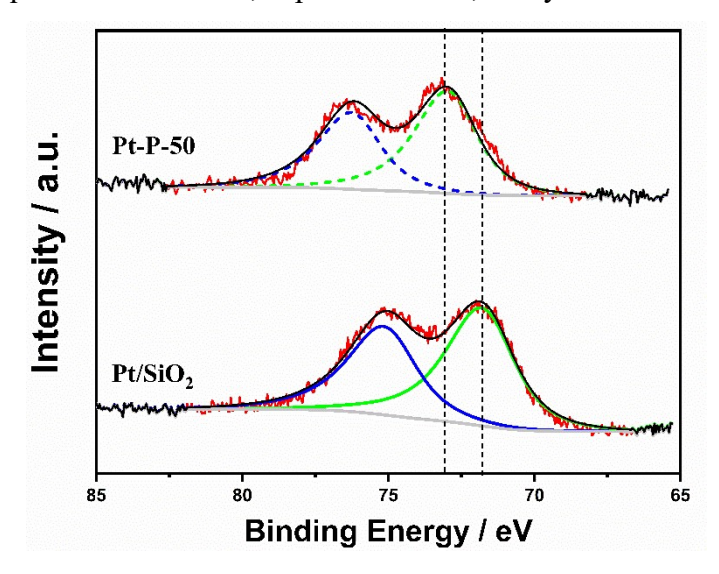


Figure 7. Pt 4f XPS spectra of catalysts after reduction at 550 °C with H₂. Raw data (red solid line), fitting curve (black solid line), Pt⁰ state: Pt 4f_{7/2} (green solid line) and Pt⁰ 4f_{5/2} (blue solid line), Pt²⁺ state: Pt 4f_{7/2} (green dash line), Pt 4f_{5/2} (blue dash line).

3.4. Determination of the Energy of the (Filled) Pt 5d Valence Orbitals. The XANES and XPS results suggest that the energy of the Pt 5d valence orbitals is significantly different from that of metallic Pt NPs. For example, the formation of PtP₂ increases the unfilled 5d orbital energies suggested by the L_{III} edge XANES. The increase in the 4f XPS binding energies also suggests a change in the energy of the Pt 5d valence orbitals. Both techniques, however, are indirect measurements of the energy of the filled 5d orbitals, which are primarily responsible for catalytic performance. To directly quantity the effect of P on the energy of the filled valence states in PtP₂, in situ Resonant Inelastic X-ray Scattering (RIXS) measurements were conducted on Pt/SiO₂ and PtP₂/SiO₂ (Pt-P-50), i.e., where every Pt atom has the same structure. The energy difference between the unfilled and filled Pt 5d states was determined by the measurements of L₃ absorption edge and Lβ₅ emission lines. Figure 8 shows the experimentally measured RIXS spectra for Pt/SiO₂ and PtP₂/SiO₂ as 2-D contour plot maps, where the energy transfer (Δ E), or the difference in average energy of the filled and unfilled 5d orbitals, is a function of the incident photon energy (Ω). The location of maximum intensity can be used to determine the difference between the average energies of the filled and unfilled 5d orbitals. The maximum intensity of Pt catalysts occurs

at $\Omega = 11564.4$ eV with ΔE of 2.7 eV in accordance with literature.⁶¹ Upon forming PtP₂, the maximum RIXS intensity shifts to higher Ω of 11567.0 eV and higher energy transfer, ca. $\Delta E \sim 5.7$ eV, 3.0 eV larger than that in Pt NPs. Since the energy of unfilled valence states in PtP₂ was 1.5 eV higher than that in the monometallic Pt, determined by XANES in **Figure 6**, the energy of filled 5d valence orbitals in PtP₂ was 1.5 eV lower than that in Pt NPs. The schematics of energy level diagram for Pt 5d valence bands in Pt/SiO₂ and PtP₂/SiO₂ are shown in **Figure 9**

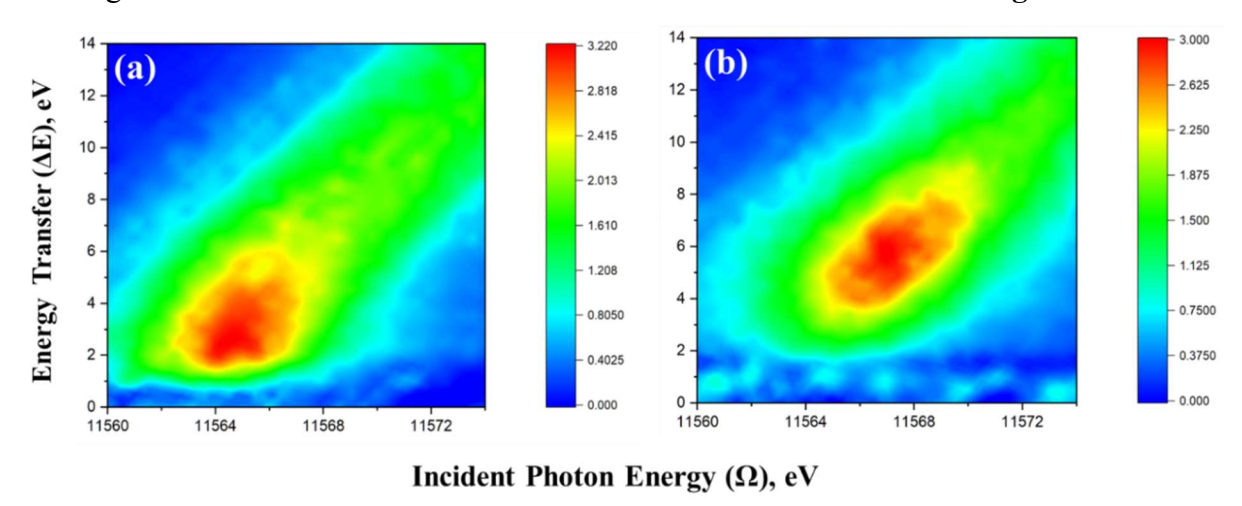


Figure 8. L₃ RIXS planes of (a) Pt/SiO₂ and (b) PtP₂/SiO₂.

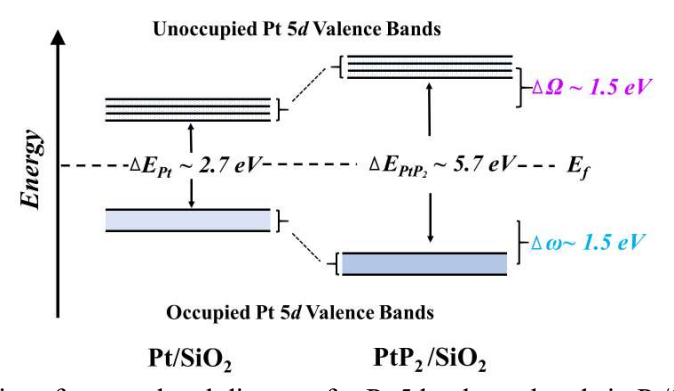


Figure 9. Schematics of energy level diagram for Pt 5d valence bands in Pt/SiO₂ and PtP₂/SiO₂

3.5. Catalytic Properties: Propane Dehydrogenation and Propylene Hydrogenation. The catalytic performance of PtP₂ and Pt NPs catalysts was determined for propylene hydrogenation and propane dehydrogenation. Since the PtP₂ did not adsorb CO at room temperature as confirmed by CO-IR (**Figure S5**), it was not possible to determine the fraction of surface Pt by standard chemisorption methods. However, the average particle size and size distributions of Pt NPs and

PtP₂ NPs (Pt-P-50) are similar, and the composition of these two catalysts have uniform compositions. Thus, the number of surface Pt sites in Pt and Pt-P-50 per gram catalyst should be very similar, and the rate per mol Pt can be used to evaluate the relative rates of Pt in these catalysts.

The rates per g of Pt for the Pt-P catalysts for propylene hydrogenation and propane dehydrogenation are given in **Table 2.** There was no propylene conversion with Pt-P-50 until the temperature was higher than about 150°C, which is consistent with other single site catalysts, for example, Co(II)⁶², Zn(II)⁶³ and Ga(III)⁶⁴; while Pt/SiO₂ has highly active at room temperature consistent with metallic Pt.⁶⁵⁻⁶⁶ The rates of Pt NPs and Pt-P-50 for hydrogenation were calculated at a conversion of ~10% at 150°C. The rate of Pt NPs is about 900 times higher than that of PtP₂ (Pt-P-50). The much lower rate of PtP₂ than metallic NPs for hydrogenation is also consistent with the rates of other single site catalysts, e.g. single site Zn(II)/SiO₂ (**Table 2**).

Table 2. Catalytic Performance in Propylene Hydrogenation at 150°C in 3% C₃H₆, 5% H₂ Balance with N₂ and Propane Dehydrogenation at 550 °C in 5% C₃H₈, 5% H₂ Balance with N₂.

Catalyst	Rate of Hydrogenation (mol _{C3H6} /mol M·s ⁻¹)	Rate of Dehydrogenation (mol _{C3H8} /mol M·s ⁻¹)	Selectivity (%) ^a	k _d (h ⁻¹)
Pt/SiO ₂	2.7	8.8×10 ⁻²	64	0.182
Pt-P-10	5.3×10 ⁻³	1.9×10 ⁻²	97	-
Pt-P-20	3.4×10 ⁻³	-	96	-
Pt-P-50	3.2×10 ⁻³	1.2×10 ⁻²	97	0.147
Zn(II)/SiO ₂ ⁶³	8.4×10 ⁻⁵	2.1×10 ⁻⁴	>95	-
Co(II)/SiO ₂ ⁶²	-	1.8×10 ⁻⁴	>95	-
Ga(III)//SiO ₂ ⁶⁴	-	5.4×10 ⁻⁴	>98	

^a Selectivity: propylene selectivity at 25% conversion of propane for Pt-P catalysts.

Since alkane dehydrogenation is the reverse reaction of olefin hydrogenation, PtP₂ catalysts were evaluated for the former reaction. The conversion and selectivity on the P/SiO₂ and SiO₂ are also shown in **Figure S9**. The performance of P/SiO₂ was almost the same as the SiO₂, which had little contribution to the catalytic performances. **Figure 10** shows the initial selectivity versus conversion of these supported Pt catalysts for PDH reactions at 550°C. The addition of H₂ to the reaction gases is a more severe test of the catalyst performance since H₂ promotes the hydrogenolysis reaction. The selectivity of the reference Pt/SiO₂ catalyst decreased rapidly from

82% to 63% as the conversion increased from 8% to 27%, which is consistent with literature. ^{4, 6} In contrast, all the Pt-P catalysts show significantly improved olefin selectivity, generally above 95%, up to ~ 30% conversion, as shown in **Figure 10**. The selectivity of these Pt catalysts at 25% conversion are listed in **Table 2** for comparison. For Pt-P-50 catalyst, the propylene selectivity remains about 97% at 25% propane conversion. The Pt-P-10 and Pt-P-20 show similar performance to Pt-P-50, where the selectivity was remains above 96% at 25% conversion, which suggests that the surface of Pt-P-10 and Pt-P-20 are likely similar to that of Pt-P-50.

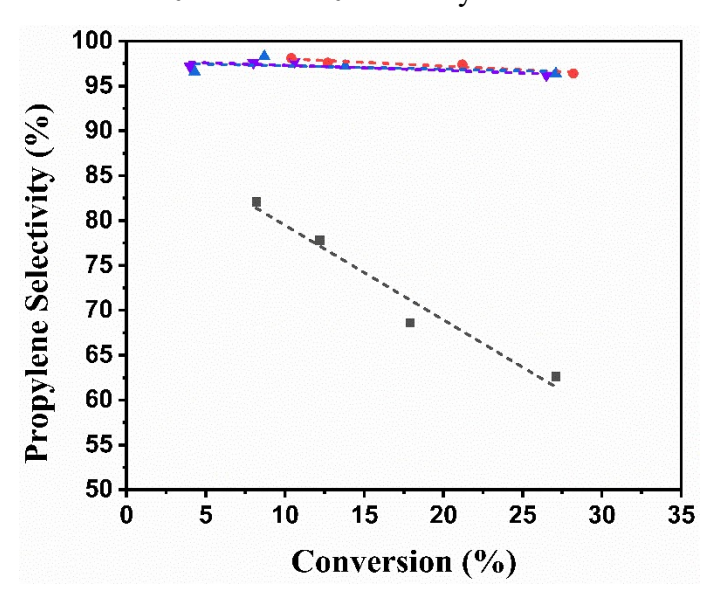


Figure 10. Initial selectivity vs. conversion in PDH after reduction at 550 °C in 5% C₃H₈, 5% H₂ balance with N₂ for Pt/SiO₂ (black), Pt-P-10 (red), Pt-P-20 (purple) and Pt-P-50 (blue).

The rates per mole Pt (based on 2 wt% Pt) for PDH were calculated at 550°C at around 10% conversion, as shown in **Table 2**. The propane conversion rate of Pt/SiO₂ is 0.088 mol C₃H₈/mol Pt s⁻¹, is about 7 times higher than 0.012 mol C₃H₈/mol Pt s⁻¹ of PtP₂ (Pt-P-50) catalyst. The lower rates and high selectivity of Pt-P catalysts are again consistent with the reported transition metal^{62, 64, 67} and main group^{62, 64, 67} single site catalysts, as shown in **Table 2**

The stability of Pt and PtP₂ (Pt-P-50) were also evaluated assuming a first-order deactivation mechanism, and the deactivation rate constants (k_d) are listed in **Table 2**. **Figure S10** shows the propane conversion versus time-on-stream over Pt NPs and Pt-P-50 catalysts, where the initial conversion of both catalysts was ~28%. For both Pt NPs and Pt-P-50, the conversion declined rapidly over the first 30 minutes, and stabilized after 5 h. The k_d of Pt-P-20 is 0.147 h⁻¹, which is slightly lower than 0.182 h⁻¹ of Pt NPs. The synthesis conditions of PtP₂ has not been optimized

for deactivation and alkali addition to other metal phosphides has been shown to reduce acid sites from excess phosphate and improve conversion stability.⁶⁸⁻⁶⁹

3.6. Acetylene Selective Hydrogenation. Hydrogenation of acetylene yields ethylene which can be further hydrogenated to ethane. A selective catalyst will be able to provide high concentrations of ethylene. The selectivity defined in equation (6) of the experimental section and indicates the ability of the catalyst to suppress the over hydrogenation to form ethane. 1 wt% Pd/Alumina was used as a reference catalyst since Pd is known to be effective for selective hydrogenation acetylene to ethylene for production of polymer grade ethylene, for example. 70 On the other hand, metallic Pt is not known to be highly selective for acetylene hydrogenation. Figure 11a shows the conversion of acetylene as a function of temperature and increasing conversion. Figure S11 shows the concentrations of acetylene, ethylene and ethane for each catalyst, and the ethylene selectivity ethylene as a function of acetylene conversion is shown in Figure 11b. Metallic Pt is active at temperatures from 40-140°C, but the selectivity to ethylene is low and shows a monotonic decrease with increasing conversion. For the PtP₂ catalysts, hydrogenation occurs at higher temperatures due to its lower intrinsic activity, but the ethylene selectivity is significantly higher than Pt and even Pd NPs. In addition, the selectivity remains high at higher conversions. Table 3 shows the selectivity of these catalysts at 50% conversion of acetylene, showing the improvement attained with the PtP₂ catalysts. The loss in selectivity for Pt NPs can be attributed to the strong binding of ethylene on metallic Pt with facile hydrogenation to form ethane. While in the case of PtP₂ where Pt in the +2 oxidation state, the weaker binding of ethylene allows it to desorb, leading to improved overall selectivity of the catalyst. Figure 11b clearly shows that the PtP₂ catalysts retain their selectivity towards ethylene at high conversions of acetylene, which is required since acetylene is a poison for the downstream polymerization catalysts.71

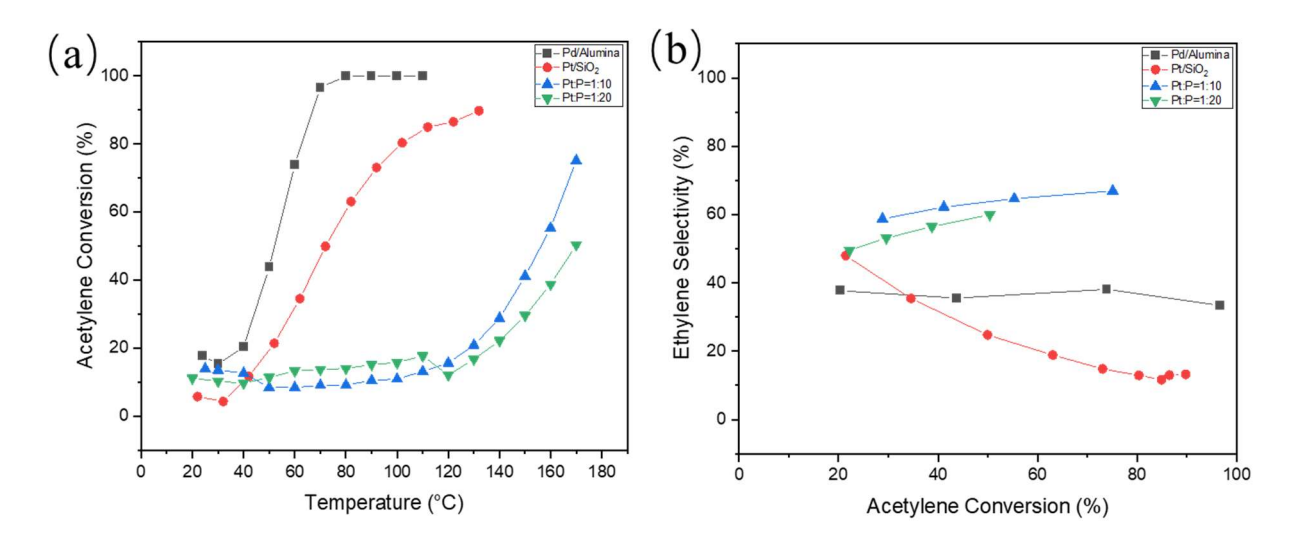


Figure 11. The catalyst Pd/Al₂O₃ (grey), Pt/SiO₂ (red), Pt-P-10 (blue) and Pt-P-20 (green) was reduced in 4% H₂ balance with N₂ at 350°C for 60 mins then a feed stream of 1% C₂H₂, 4% H₂ and rest balanced with N₂ for selective acetylene hydrogenation. (a) Acetylene conversion as a function of Temperature (b) Ethylene selectivity as a function of Acetylene conversion.

Table 3 Catalytic Results of Selective Acetylene Hydrogenation

Catalyst	T ₅₀ (°C) ^a	Ethylene Selectivity (%) ^b
Pd/Al ₂ O ₃	52	36
Pt/SiO ₂	72	25
Pt-P-10	155	63
Pt-P-20	170	60

^a Catalyst bed outlet temperature for 50% acetylene conversion

4 DISCUSSION

4.1. Synthesis and Formation of PtP₂. The synthesis of PtP₂ was previous prepared by dissociating an organometallic precursor at 1000-1100°C, resulting in large particles of ~50 nm. ⁷² In our study, supported PtP₂ NPs with particle size of 2-3 nm were prepared with different amount of H₃PO₄ by IWI following reduction at 550°C, which is similar to industrial synthesis methods. The cheap, safe and readily available phosphorus source plus the relatively low reduction temperature are suitable for large scale preparations. After calcination, the oxidized Pt NPs were formed. The EXAFS spectrum of unreduced Pt-P-50 was well fitted with Pt-O scattering (**Figure**

^b Ethylene selectivity at 50% acetylene conversion

S12). After H₂ reduction at 550°C, the PtP₂ ordered structure was formed confirmed by EXAFS and STEM. Here, the Pt²⁺ ions in PtP₂ are formed in a high-temperature reducing environment in agreement with the reported synthesis conditions for other phosphorus-rich transition metal phosphides (MP₂/MP₃).⁷²⁻⁷⁴ During the reduction, it is likely that Pt ions dissociate H₂, which facilitates reduction of phosphate through hydrogen spillover.⁷⁵

In addition to full PtP₂, the Pt-P-10 and Pt-P-20 display core-shell structure (Pt@PtP₂) confirmed by EXAFS, sXRD, surface XAS and catalytic performance. As the P/Pt molar ratio increases from 10 to 20, the CN_{Pt-Pt} decreases from 2.4 to 1.8 and the CN_{Pt-P} increases from 3.5 to 3.7. We hypothesize that in the reducing environment, Pt NPs were initially formed, and then the phosphorus diffuses from the surface to the center of particle to form PtP₂ with Pt atoms. The more phosphorus, the more surface PtP₂ was formed until the nanoparticle consists of pure PtP₂, as shown in **Figure 12**. For all catalysts there is a large excess of P than is required for formation of PtP₂. The excess P is present at P⁵⁺ as determined by XPS. This also suggests phosphate ions, which are not near the initially formed Pt NP cannot be reduced under these conditions. The same surface of Pt@PtP₂ and pure PtP₂ NPs leads to similar catalytic performance, e.g. low rate per mole Pt (compared to Pt NPs), high olefin selectivity, no CO chemisorption capacity, *etc*.

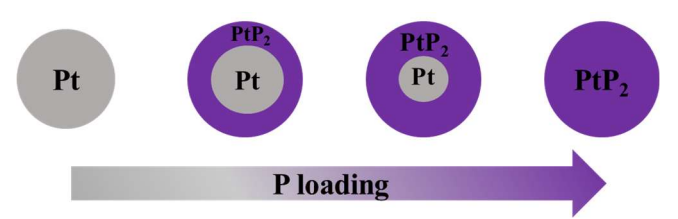


Figure 12. Schematics of the evolution of nanoparticles structure as the P loading increases.

4.2. The Nature of Surface Pt²⁺ Ions in PtP₂ NPs. Pt-P-50 has a fully-formed PtP₂ crystalline structure with Pt-P bonds at 2.36 Å confirmed by EXAFS (Figure 1) and STEM (Figure 4). As shown in Figure 13, in PtP₂ structure, Pt still adopts FCC unit cell, albeit with a much larger size than Pt NPs, with P₂²⁻ ions midway between the Pt²⁺ ions. The Pt-Pt distance is 4.02 Å, significantly longer than that in Pt NPs (2.78 Å). In the PtP₂ the distance between adjacent Pt is too long for Pt-Pt bond formation.

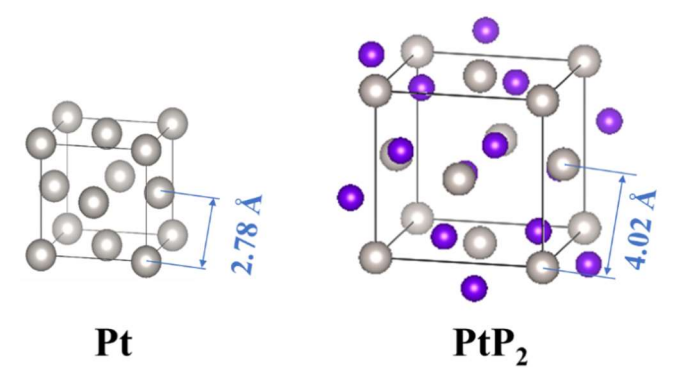


Figure 13. The unit cell of Pt FCC and PtP₂ crystalline structure (Pt atoms are represented in gray and P atoms in purple).

The increases of white line intensity and edge energy of XANES is consistent with Pt²⁺ in PtP₂, which agrees with Pt²⁺ binding energies determined by XPS. The energy of Pt valence orbitals, which form bonds with reactants and products, determines the catalytic properties. To directly quantity and compare the energy of filled 5d valence orbitals, RIXS was conducted on Pt NPs and the full phase PtP₂. RIXS is bulk technique and measures every atom in the sample. Thus, it is essential that each Pt has an identical structure. As shown in XANES spectrum, Figure 6, the formation of PtP₂ significantly increases the energy of unfilled Pt 5d orbitals by 1.5 eV. The RIXS spectrum is the difference in energy of the empty and filled Pt 5d states. Thus, there is a decrease in the energy of filled Pt 5d orbitals by 1.5 eV, Figures 8 and 9, compared to Pt NPs. Thus, the increase in the energy of unfilled orbitals is nearly the same as the decrease in the energy of the filled orbitals, which is similar to previously studied bimetallic Pt catalysts. 5-6 For comparison, the decrease in energy of the filled 5d orbitals in PtP₂ NPs are larger than those observed for many bimetallic Pt catalysts, for example, 1.1 eV shift in Pt₁Zn₁⁵ and 0.4 eV shift in Pt₃V⁶¹ catalysts. This decrease in the energy of the filled 5d orbitals in PtP₂ would be expected to lead to significantly weaker Pt-adsorbate and reaction intermediate bond energies compared to metallic Pt.

4.3. Structure-Property Relationship and Implications for Catalysis. Pt is one of the most versatile catalytic elements with applications to both oxidation and reduction reactions, for example, hydrocarbon and CO oxidation, olefin hydrogenation, naphtha reforming, fuel cells, electrocatalysis, etc.^{1, 76} In each of these, metallic Pt is the active phase. Although phosphorous-rich metal phosphides are known, currently all catalytically active transition metal phosphides are

metal-rich and possess metallic properties.^{35, 38} Metal-rich transition metal phosphides have MP and M₂P structures. For example, Oyama et al⁴⁰ has compared the hydrodesulfurization (HDS), hydrodenitrogenation (HDN) and hydrodeoxygenation (HDO) activity for a series of metal phosphide catalysts and the activity was in the order, Fe₂P<CoP<MoP<WP<Ni₂P. By comparison, PtP₂ was much less active that other metal phosphides catalysts; although the reason for the very low activity was not known.³⁹ As shown above, PtP₂, is not metallic and doesn't show catalytic or chemisorption properties typical of Pt NP's. For example, PtP₂ does not hydrogenate olefins at low temperature, chemisorb CO or is not oxidized by air at low temperature. The Pt²⁺ surface ions, however, catalyze olefin hydrogenation but at much higher temperature than Pt NPs, and will affect alkane dehydrogenation, albeit at a lower turnover rate than metallic Pt. While PtP2 has a lower rate than Pt NPs, it does have significantly improved selectivity. For propane dehydrogenation, Pt is poorly selective, ca. 65% at 20% conversion, while the olefin selectivity of PtP₂ is greater than 95% at the same conversion. Similarly, the selectivity for acetylene hydrogenation to ethylene is much higher for PtP₂ than Pt NP's. The catalytic properties of PtP₂ is less like those of Pt NP's and more similar to those of single site, ionic catalysts, for example, single site Co(II)⁶², Zn(II)⁶³ and Ga(III)⁶⁴ ions on silica and Ga^{26, 77} and Cr⁷⁸ on alumina. For the latter, however, the structures and composition of the catalytic sites are significantly different from that in PtP₂. In the transition and main group catalysts the active site is a low coordinate, isolated ion bonded to and stabilized by the support, i.e., a metal ion is bonded through support O ions. For all the non-metallic dehydrogenation catalysts, the oxides are not reduced to metallic NPs at the high reaction temperatures. In PtP₂, while the Pt²⁺ ions are isolated from other Pt ions, i.e., no Pt-Pt bonds, they are not bonded to the support but are present in a nano-particle. Thus, for the maximum rate, it is necessary to synthesis small NPs. Similar to the active sites in Zn(II)^{63, 79}, Co(II)⁶², Ga(III)⁶⁴, and Fe(II)⁸⁰ single site catalysts, PtP₂ does not reduce to metallic NPs due to stabilization of the Pt2+ ions by the P22- ions. Thus, PtP2 can be used for high temperature hydrogenation reactions.

Single site Zn(II)^{63, 79}, Co(II)⁶², Ga(III)⁶⁴, and Fe(II)⁸⁰ supported on silica catalysts also show olefin selectivities above about 95% and often with little coke formation or lower deactivation rates than for bimetallic alloy NPs.^{63, 80} Although non-metallic dehydrogenation catalysts have high olefin selectivity and, generally, suppressed coke formation, a limitation of these catalysts is their lower rate compared to metallic catalysts. The olefin hydrogenation and alkane

dehydrogenation rates of Pt^{2+} in PtP_2 are about 40 and 90 times higher, respectively, than that for $Zn(II)/SiO_2$ single site catalysts, **Table 2**. For the latter all sites are active; while in PtP_2 about 40% of the Pt would be at the surface of the 2.5 nm particles. Thus, the TORs of Pt^{2+} are approximately 100 times higher olefin hydrogenation and over 200 times higher for propane dehydrogenation than that of $Zn(II)/SiO_2$.

The difference in adsorption energies, reaction rates and selectivity compared to metallic Pt NPs also suggests that PtP₂ catalysts may find different catalytic applications than the former. The results for selective hydrogenation of acetylene over ethylene is consistent with this suggestion. Although Pt NPs are highly active for acetylene and ethylene hydrogenation, the poor selectivity is likely to due to strong bonding of the product ethylene to metallic Pt and high surface coverage of activated hydrogen leads to the over hydrogenation of the ethylene (to ethane) resulting in poor selectivity. For PtP₂ the isolated Pt²⁺ leads to weak bonding of the ethylene and also low hydrogen coverage of the NP resulting in improved selectivity.

The development of new, single site, ionic catalytic materials for a variety of catalytic applications in electro-catalysis, photo-catalysis, thermal catalysis, etc., is an active area of research. 81-82 These often display catalytic properties, which are distinct from those of metal NPs. For these catalysts, the ions are generally stabilized by the oxide, carbon or carbon-nitrogen support. 83-85 Here we show that active single site ions present in nano-particles with chemically stable molecular structures can also be considered possible new materials for these and other reactions. While further improvements in rate, selectivity and stability may be required for technological applications for PtP₂, the results do demonstrate the opportunity for better performance for some reactions compared to metallic Pt NPs. The future chemistry of PtP₂ and similar nano-particle single site, ionic catalysts remains to be explored, but it is anticipated that the preferred reactions will be different from those of metallic NPs.

5. CONCLUSION

Silica supported 2-3 nm PtP₂ NPs were successfully synthesized using a simple and scalable IWI method. In the PtP₂ NPs, the Pt²⁺ ions are separated by P₂²⁻ ions, i.e., no Pt-Pt bonds, unlike other Group 8, catalytic metal phosphide catalysts, e.g., Ni, Fe, Ru, Rh, etc. In PtP₂, the energy of the filled Pt 5d valence orbitals is about 1.5 eV lower than in metallic Pt NPs. These electronic effects lead to a decrease in bond strength of adsorbates, for example CO and reaction

intermediates, lowering the rates but also improving the selectivity. The PtP₂ catalytic surface exhibits very low hydrogenation rates nearly 1000 times lower than metallic Pt requiring higher reaction temperatures. At higher temperatures, the propane dehydrogenation the rate per Pt in PtP₂ is about 7 times lower than that in Pt NPs; however, the former has excellent olefin selectivity compared to the latter. The difference in rates and selectivity suggest that PtP₂ will find different applications to those of Pt NPs as demonstrated by the selective hydrogenation of acetylene. The isolated Pt²⁺ ions have a significantly higher turnover rate than other ionic and alloy single site catalysts, thus, may have potential for similar applications of the latter.

ACKNOWLEDGEMENT

JK, LG were supported by the Basic Science Center Program for Ordered Energy Conversion of the National Natural Science Foundation of China (No.51888103). JK also wishes to thank the China Scholarship Council (201806280119). JZC, GZ, AG, AKD and JTM were supported in part by the National Science Foundation under Cooperative Agreement No. EEC-1647722. JG, DZ and JTM were supported by National Science Foundation under award CBET-1804712. AG and AD were supported by NSF GOALI grant CBET 1707127. GZ would like to acknowledge the National Natural Science Foundation of China (21902019) and Fundamental Research Funds for the Central Universities (DUT20RC(5)002). WL acknowledge the CAS Youth Innovation Promotion Association (2019190). RM would like to thank Chemistry and Chemical Engineering Guangdong Laboratory for a startup funding support (2111001). AJK was supported by the U.S. Department of Energy (DOE), Office of Basic Energy Sciences, Division of Chemical Sciences, Geosciences, and Biosciences, Catalysis Science Program under Contract DE-AC02-06CH11357 (Argonne National Laboratory). Use of the Advanced Photon Source was supported by the U.S. Department of Energy Office of Basic Energy Sciences under contract no. DE-AC02-06CH11357. MRCAT operations, beamlines 10-BM and 10-ID, are supported by the Department of Energy and the MRCAT member institutions. The authors also acknowledge the use of beamline 11-ID-C.

REFERENCES

- (1) Yu, W.; Porosoff, M. D.; Chen, J. G., Review of Pt-Based Bimetallic Catalysis: From Model Surfaces to Supported Catalysts. *Chem. Rev.* **2012**, *112*, 5780-5817.
- (2) Cortright, R.; Dumesic, J., Effects of potassium on silica-supported Pt and Pt/Sn catalysts for isobutane dehydrogenation. *J. Catal.* **1995**, *157*, 576-583.

- (3) Sattler, J. J.; Ruiz-Martinez, J.; Santillan-Jimenez, E.; Weckhuysen, B. M., Catalytic dehydrogenation of light alkanes on metals and metal oxides. *Chem. Rev.* **2014**, *114*, 10613-10653.
- (4) LiBretto, N. J.; Yang, C.; Ren, Y.; Zhang, G.; Miller, J. T., Identification of Surface Structures in Pt₃Cr Intermetallic Nanocatalysts. *Chem. Mater.* **2019**, *31*, 1597-1609.
- (5) Cybulskis, V. J.; Bukowski, B. C.; Tseng, H.-T.; Gallagher, J. R.; Wu, Z.; Wegener, E.; Kropf, A. J.; Ravel, B.; Ribeiro, F. H.; Greeley, J., Zinc Promotion of platinum for catalytic light alkane dehydrogenation: insights into geometric and electronic effects. *ACS catal.* **2017**, *7*, 4173-4181.
- (6) Cesar, L. G.; Yang, C.; Lu, Z.; Ren, Y.; Zhang, G.; Miller, J. T., Identification of a Pt₃Co Surface Intermetallic Alloy in Pt-Co Propane Dehydrogenation Catalysts. *ACS catal.* **2019**, *9*, 5231-5244.
- (7) ZhuChen, J.; Wu, Z.; Zhang, X.; Choi, S.; Xiao, Y.; Varma, A.; Liu, W.; Zhang, G.; Miller, J. T., Identification of the Structure of the Bi Promoted Pt Non-oxidative Coupling of Methane Catalyst: A Nanoscale Pt₃Bi Intermetallic Alloy. *Catal. Sci. Technol.* **2019**, *9*, 1349-1356.
- (8) Ye, C.; Wu, Z.; Liu, W.; Ren, Y.; Zhang, G.; Miller, J. T., Structure Determination of a Surface Tetragonal Pt₁Sb₁ Phase on Pt Nanoparticles. *Chem. Mater.* **2018**, *30*, 4503-4507.
- (9) Wegener, E. C.; Wu, Z.; Tseng, H.-T.; Gallagher, J. R.; Ren, Y.; Diaz, R. E.; Ribeiro, F. H.; Miller, J. T., Structure and reactivity of Pt–In intermetallic alloy nanoparticles: Highly selective catalysts for ethane dehydrogenation. *Catal. Today* **2018**, *299*, 146-153.
- (10) Zhu, H.; Anjum, D. H.; Wang, Q.; Abou-Hamad, E.; Emsley, L.; Dong, H.; Laveille, P.; Li, L.; Samal, A. K.; Basset, J.-M., Sn surface-enriched Pt–Sn bimetallic nanoparticles as a selective and stable catalyst for propane dehydrogenation. *J. Catal.* **2014**, *320*, 52-62.
- (11) Chen, S.; Chang, X.; Sun, G.; Zhang, T.; Xu, Y.; Wang, Y.; Pei, C.; Gong, J., Propane dehydrogenation: catalyst development, new chemistry, and emerging technologies. *Chem. Soc. Rev.* **2021**, *50*, 3315-3354.
- (12) Rahimpour, M. R.; Jafari, M.; Iranshahi, D., Progress in catalytic naphtha reforming process: A review. *Applied Energy* **2013**, *109*, 79-93.
- (13) Ciapetta, F. G.; Wallace, D. N., Catalytic Naphtha Reforming. Ctalysis Reviews: 1972; Vol. 5.
- (14) Schweitzer, N. M.; Schaidle, J. A.; Ezekoye, O. K.; Pan, X.; Linic, S.; Thompson, L. T., High activity carbide supported catalysts for water gas shift. *Journal of the American Chemical Society* **2011**, *133*, 2378.
- (15) Li, Y.; Kottwitz, M.; Vincent, J. L.; Enright, M. J.; Frenkel, A. I., Dynamic structure of active sites in ceria-supported Pt catalysts for the water gas shift reaction. *Nat. Commun.* **2021**, *12*.
- (16) Cortright, R. D.; Davda, R. R.; Dumesic, J. A., Hydrogen from catalytic reforming of biomass-derived hydrocarbons in liquid water. *Nature* **2002**, *418*, 964-967.
- (17) Shelef, M.; Mccabe, R. W., Twenty-five years after introduction of automotive catalysts: what next? *Catal. Today* **2000**, *62*, 35-50.
- (18) Farrauto, R. J.; Heck, R. M., Catalytic converters: state of the art and perspectives. *Catal. Today* **1999**, *51*, 351-360.
- (19) Sheng, S.; Wang, X.; Zhou, X.; Su, Y.; Riffat, S.; Liu, C. J., A comprehensive review of Pt electrocatalysts for the oxygen reduction reaction: Nanostructure, activity, mechanism and carbon support in PEM fuel cells. *J. Mater. Chem. A* **2017**, *5*.
- (20) Zhu, J.; Hu, L.; Zhao, P.; Lee, L.; Wong, K. Y., Recent Advances in Electrocatalytic Hydrogen Evolution Using Nanoparticles. *Chem. Rev.* **2019**, *120*.
- (21) Shrestha, S.; Liu, Y.; Mustain, W. E., Electrocatalytic Activity and Stability of Pt clusters on State-of-the-Art Supports: A Review. *Cat. Rev. Sci. Eng.* **2011**, *53*, 256-336.
- (22) Bariås, O. A.; Holmen, A.; Blekkan, E. A., Propane dehydrogenation over supported Pt and Pt–Sn catalysts: catalyst preparation, characterization, and activity measurements. *J. Catal.* **1996**, *158*, 1-12.
- (23) Zhang, Y.; Zhou, Y.; Qiu, A.; Wang, Y.; Xu, Y.; Wu, P., Propane dehydrogenation on PtSn/ZSM-5 catalyst: Effect of tin as a promoter. *Catal. Commun.* **2006**, *7*, 860-866.
- (24) Airaksinen, S. M. K.; Harlin, M. E.; Krause, A. O. I., Kinetic modeling of dehydrogenation of isobutane on chromia/alumina catalyst. *Industrial & Engineering Chemistry Research* **2002**, *41*, 5619-5626.
- (25) Puurunen, R. L.; Weckhuysen, B. M., Spectroscopic study on the irreversible deactivation of chromia/alumina dehydrogenation catalysts. *J. Catal.* **2002**, *210*, 418-430.

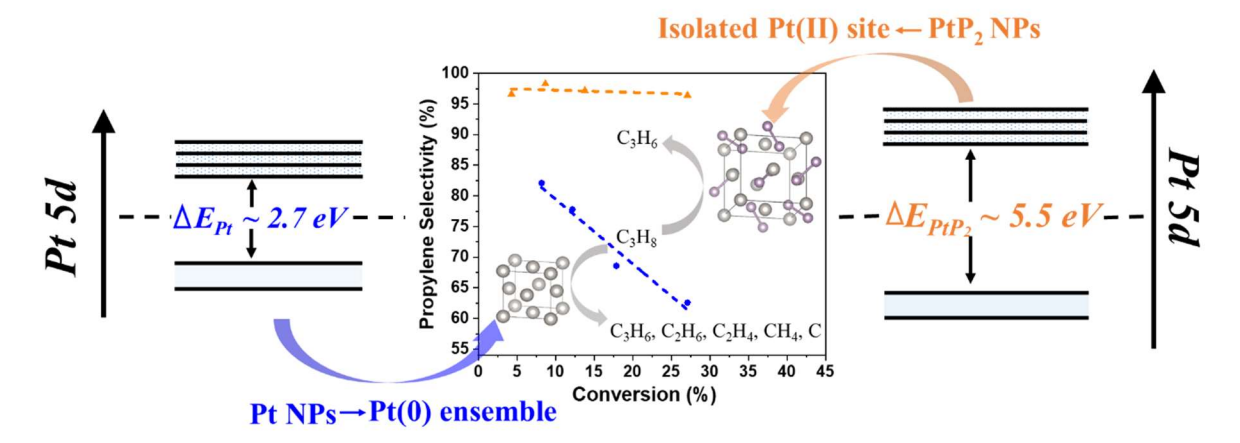
- (26) Sattler, J. J. H. B.; Gonzalez-Jimenez, I. D.; Luo, L.; Stears, B. A.; Malek, A.; Barton, D. G.; Kilos, B. A.; Kaminsky, M. P.; Verhoeven, T. W. G. M.; Koers, E. J.; Baldus, M.; Weckhuysen, B. M., Platinum-Promoted Ga/Al2O3 as Highly Active, Selective, and Stable Catalyst for the Dehydrogenation of Propane. *Angewandte Chemie-International Edition* **2014**, *53*, 9251-9256.
- (27) Prins, R.; Bussell, M. E., Metal phosphides: preparation, characterization and catalytic reactivity. *Catal. Lett.* **2012**, *142*, 1413-1436.
- (28) Yuan, C.-Z.; Hui, K. S.; Yin, H.; Zhu, S.; Zhang, J.; Wu, X.-L.; Hong, X.; Zhou, W.; Fan, X.; Bin, F.; Chen, F.; Hui, K. N., Regulating Intrinsic Electronic Structures of Transition-Metal-Based Catalysts and the Potential Applications for Electrocatalytic Water Splitting. *Acs Materials Letters* **2021**, *3*, 752-780.
- (29) El-Refaei, S. M.; Russo, P. A.; Pinna, N., Recent Advances in Multimetal and Doped Transition-Metal Phosphides for the Hydrogen Evolution Reaction at Different pH values. *ACS applied materials & interfaces* **2021**, *13*, 22077-22097.
- (30) Shi, Y.; Li, M.; Yu, Y.; Zhang, B., Recent advances in nanostructured transition metal phosphides: synthesis and energy-related applications. *Energy & Environmental Science* **2020**, *13*, 4564-4582.
- (31) Pu, Z.; Liu, T.; Amiinu, I. S.; Cheng, R.; Mu, S., Transition-metal Phosphides: Activity Origin, Energy-related Electrocatalysis Applications and Synthetic Strategies. *Adv. Funct. Mater.* **2020**.
- (32) Alvarado Rupflin, L.; Boscagli, C.; Schunk, S. A., Platinum Group Metal Phosphides as Efficient Catalysts in Hydroprocessing and Syngas-Related Catalysis. *Catalysts* **2018**, *8*, 122.
- (33) Feng, L.; Xue, H., Advances in Transition-Metal Phosphide Applications in Electrochemical Energy Storage and Catalysis. *Chemelectrochem* **2017**, *4*, 20-34.
- (34) Liu, K.; Zhang, C.; Sun, Y.; Zhang, G.; Shen, X.; Zou, F.; Zhang, H.; Wu, Z.; Wegener, E. C.; Taubert, C. J., High-performance transition metal phosphide alloy catalyst for oxygen evolution reaction. *ACS nano* **2018**, *12*, 158-167.
- (35) Shi, Y.; Zhang, B., Recent advances in transition metal phosphide nanomaterials: synthesis and applications in hydrogen evolution reaction. *Chem. Soc. Rev.* **2016**, *45*, 1529-1541.
- (36) Pei, Y.; Cheng, Y.; Chen, J.; Smith, W.; Dong, P.; Ajayan, P. M.; Ye, M.; Shen, J., Recent developments of transition metal phosphides as catalysts in the energy conversion field. *J. Mater. Chem. A* **2018**, *6*, 23220-23243.
- (37) Zhao, H.; Li, D.; Bui, P.; Oyama, S., Hydrodeoxygenation of guaiacol as model compound for pyrolysis oil on transition metal phosphide hydroprocessing catalysts. *Appl. Catal. A: Gen.* **2011,** *391*, 305-310.
- (38) Oyama, S. T.; Gott, T.; Zhao, H.; Lee, Y.-K., Transition metal phosphide hydroprocessing catalysts: A review. *Catal. Today* **2009**, *143*, 94-107.
- (39) Kanda, Y.; Temma, C.; Nakata, K.; Kobayashi, T.; Sugioka, M.; Uemichi, Y., Preparation and performance of noble metal phosphides supported on silica as new hydrodesulfurization catalysts. *Appl. Catal. A: Gen.* **2010**, *386*, 171-178.
- (40) Oyama, S. T., Novel catalysts for advanced hydroprocessing: transition metal phosphides. *J. Catal.* **2003**, *216*, 343-352.
- (41) Rupflin, L. A.; Mormul, J.; Lejkowski, M.; Titlbach, S.; Papp, R.; Glaeser, R.; Dimitrakopoulou, M.; Huang, X.; Trunschke, A.; Willinger, M. G.; Schloegl, R.; Rosowski, F.; Schunk, S. A., Platinum Group Metal Phosphides as Heterogeneous Catalysts for the Gas-Phase Hydroformylation of Small Olefins. *ACS catal.* **2017**, *7*, 3584-3590.
- (42) Ko, J.; Muhlenkamp, J. A.; Bonita, Y.; LiBretto, N. J.; Miller, J. T.; Hicks, J. C.; Schneider, W. F., Experimental and Computational Investigation of the Role of P in Moderating Ethane Dehydrogenation Performance over Ni-Based Catalysts. *Industrial & Engineering Chemistry Research* **2020**, *59*, 12666-12676.
- (43) Yao, Y.; Zuo, M.; Zhou, H.; Li, J.; Shao, H.; Jiang, T.; Liao, X.; Lu, S., One-Pot Preparation of Ni₂P/γ-Al₂O₃ Catalyst for Dehydrogenation of Propane to Propylene. *ChemistrySelect* **2018**, *3*, 10532-10536.
- (44) Zhu, Q.; Zhang, H.; Zhang, S.; Wang, G.; Zhu, X.; Li, C., Dehydrogenation of Isobutane over a Ni–P/SiO₂ Catalyst: Effect of P Addition. *Industrial & Engineering Chemistry Research* **2019**, *58*, 7834-7843.

- (45) Li, J.; Chai, Y.; Liu, B.; Wu, Y.; Li, X.; Tang, Z.; Liu, Y.; Liu, C., The catalytic performance of Ni₂P/Al₂O₃ catalyst in comparison with Ni/Al₂O₃ catalyst in dehydrogenation of cyclohexane. *Appl. Catal. A: Gen.* **2014**, *469*, 434-441.
- (46) Xu, Y.; Wang, X.; Lv, R., Interaction between Cs and Ni₂P/SiO₂ for enhancing isobutane dehydrogenation in the presence of hydrogen. *Reaction Kinetics, Mechanisms and Catalysis* **2014**, *113*, 393-406.
- (47) Ma, R.; Yang, T.; Gao, J.; Kou, J.; Zhu Chen, J.; He, Y.; Miller, J. T.; Li, D., Composition tuning of Ru-based phosphide for enhanced propane selective dehydrogenation. *ACS catal.* **2020**.
- (48) Ravel, B.; Newville, M., Athena, artemis, hephaestus: data analysis for X-ray absorption spectroscopy using IFEFFIT. *J. Synchrotron Radiat.* **2005**, *12*, 537-541.
- (49) Hammersley, A.; Svensson, S.; Hanfland, M.; Fitch, A.; Hausermann, D., Two-dimensional detector software: from real detector to idealised image or two-theta scan. *High Press. Res.* **1996**, *14*, 235-248.
- (50) Lutterotti, L.; Matthies, S.; Wenk, H.-R.; Schultz, A.; Richardson Jr, J., Combined texture and structure analysis of deformed limestone from time-of-flight neutron diffraction spectra. *J. Appl. Phys.* **1997**, *81*, 594-600.
- (51) Bolin, T. B.; Wu, T.; Schweitzer, N.; Lobo-Lapidus, R.; Kropf, A. J.; Wang, H.; Hu, Y.; Miller, J. T.; Heald, S. M., In situ intermediate-energy X-ray catalysis research at the advanced photon source beamline 9-BM. *Catal. Today* **2013**, *205*, 141-147.
- (52) Read, C. G.; Callejas, J. F.; Holder, C. F.; Schaak, R. E., General strategy for the synthesis of transition metal phosphide films for electrocatalytic hydrogen and oxygen evolution. *ACS applied materials & interfaces* **2016**, *8*, 12798-12803.
- (53) Popczun, E. J.; McKone, J. R.; Read, C. G.; Biacchi, A. J.; Wiltrout, A. M.; Lewis, N. S.; Schaak, R. E., Nanostructured nickel phosphide as an electrocatalyst for the hydrogen evolution reaction. *Journal of the American Chemical Society* **2013**, *135*, 9267-9270.
- (54) Li, J.; Li, J.; Zhou, X.; Xia, Z.; Gao, W.; Ma, Y.; Qu, Y., Highly efficient and robust nickel phosphides as bifunctional electrocatalysts for overall water-splitting. *ACS applied materials & interfaces* **2016**, *8*, 10826-10834.
- (55) Miller, J. T.; Schreier, M.; Kropf, A. J.; Regalbuto, J. R., A fundamental study of platinum tetraammine impregnation of silica: 2. The effect of method of preparation, loading, and calcination temperature on (reduced) particle size. *J. Catal.* **2004**, *225*, 203-212.
- (56) Miller, J.; Kropf, A.; Zha, Y.; Regalbuto, J.; Delannoy, L.; Louis, C.; Bus, E.; van Bokhoven, J. A., The effect of gold particle size on AuAu bond length and reactivity toward oxygen in supported catalysts. *J. Catal.* **2006**, *240*, 222-234.
- (57) Wu, Z.; Bukowski, B. C.; Li, Z.; Milligan, C.; Zhou, L.; Ma, T.; Wu, Y.; Ren, Y.; Ribeiro, F. H.; Delgass, W. N., Changes in catalytic and adsorptive properties of 2 nm Pt₃Mn nanoparticles by subsurface atoms. *Journal of the American Chemical Society* **2018**, *140*, 14870-14877.
- (58) Fung, S. C., XPS studies of strong metal-support interactions (SMSI)-Pt/TiO₂. J. Catal. 1982, 76.
- (59) Dake; L., S., Auger parameter measurements of phosphorus compounds for characterization of phosphazenes. *Journal of Vacuum Science & Technology A Vacuum Surfaces and Films* **1989,** 7, 1634-1638.
- (60) Vasiliy; V.; Pryadchenko; Vasiliy; V.; Srabionyan; Leon; A.; Avakyan; Jeroen, Electronic Structure of Pt and Au Compounds Measured by X-ray Emission and X-ray Absorption Spectroscopies. *The Journal of Physical Chemistry C* **2012**, *116*.
- (61) Purdy, S.; Ghanekar, P.; Mitchell, G. M.; Kropf, A. J.; Zemlyanov, D. Y.; Ren, Y.; Ribeiro, F. H.; Delgass, W. N.; Greeley, J. P.; Miller, J. T., The Origin of Electronic Modification of Platinum in a Pt₃V Alloy and Their Consequences for Propane Dehydrogenation Catalysis. *ACS Appl. Energy Mater.* **2020**.
- (62) Hu, B.; Schweitzer, N. M.; Das, U.; Kim, H.; Niklas, J.; Poluektov, O.; Curtiss, L. A.; Stair, P. C.; Miller, J. T.; Hock, A. S., Selective propane dehydrogenation with single-site CoII on SiO₂ by a non-redox mechanism. *J. Catal.* **2015**, *322*, 24-37.

- (63) Schweitzer, N. M.; Hu, B.; Das, U.; Kim, H.; Greeley, J.; Curtiss, L. A.; Stair, P. C.; Miller, J. T.; Hock, A. S., Propylene hydrogenation and propane dehydrogenation by a single-site Zn²⁺ on silica catalyst. *ACS catal.* **2014**, *4*, 1091-1098.
- (64) Cybulskis, V. J.; Pradhan, S. U.; Lovón-Quintana, J. J.; Hock, A. S.; Hu, B.; Zhang, G.; Delgass, W. N.; Ribeiro, F. H.; Miller, J. T., The Nature of the Isolated Gallium Active Center for Propane Dehydrogenation on Ga/SiO₂. *Catal. Lett.* **2017**, *147*, 1252-1262.
- (65) Hu, C.; Shao, M.; Xiang, M.; Li, S.; Xu, S., The role of hydrogen coverage and location in 1,3-butadiene hydrogenation over Pt/SiO₂. *Reaction Chemistry & Engineering* **2019**, *5*.
- (66) Jugnet, Y.; Sedrati, R.; Bertolini, J. C., Selective hydrogenation of 1,3-butadiene on Pt 3Sn(111) alloys: comparison to Pt(111). *J. Catal.* **2005**, *229*, 252-258.
- (67) Searles, K.; Siddiqi, G.; Safonova, O. V.; Copéret, C., Silica-supported isolated gallium sites as highly active, selective and stable propane dehydrogenation catalysts. *Chem. Sci.* **2017**, *8*, 2661-2666.
- (68) Xu, Y.; Wang, X.; Lv, R., Interaction between Cs and Ni2P/SiO2 for enhancing isobutane dehydrogenation in the presence of hydrogen. *Reaction Kinetics Mechanisms and Catalysis* **2014**, *113*, 393-406.
- (69) Xu, Y.; Sang, H.; Wang, K.; Wang, X., Catalytic dehydrogenation of isobutane in the presence of hydrogen over Cs-modified Ni₂P supported on active carbon. *Appl. Surf. Sci.* **2014**, *316*, 163-170.
- (70) Bond, G. C.; Dowden, D. A.; Mackenzie, N., The selective hydrogenation of acetylene. *Transactions of the Faraday Society* **1958**, *54*, 1537-1546.
- (71) Than, C. N.; Didillon, B.; Sarrazin, P.; Cameron, C., Catalytic hydrogenation process and a catalyst for use in the process. *US* **1999**.
- (72) George, P.; Gedanken, A.; Gabashvili, A., Synthesis of stable spherical platinum diphosphide, PtP₂/carbon nanocomposite by reacting Pt (PPh₃) ₄ at elevated temperature under autogenic pressure. *Mater. Res. Bull.* **2007**, *42*, 626-632.
- (73) Coleman Jr, N.; Lovander, M. D.; Leddy, J.; Gillan, E. G., Phosphorus-rich metal phosphides: direct and tin flux-assisted synthesis and evaluation as hydrogen evolution electrocatalysts. *Inorg. Chem.* **2019**, *58*, 5013-5024.
- (74) Jiang, J.; Wang, C.; Zhang, J.; Wang, W.; Zhou, X.; Pan, B.; Tang, K.; Zuo, J.; Yang, Q., Synthesis of FeP₂/C nanohybrids and their performance for hydrogen evolution reaction. *J. Mater. Chem. A* **2015**, *3*, 499-503.
- (75) Prins, R., Hydrogen spillover. Facts and fiction. Chem. Rev. 2012, 112, 2714-2738.
- (76) Li, X.; Zhou, J.; Huang, J.; Bu, T.; Ma, Y., ADVANCES OF Pt CATALYSTS FOR PROPANE CATALYTIC DEHYDROGENATION TO PROPYLENE. *Petroleum Processing and Petrochemicals* **2019,** *50*, 102-108.
- (77) Otroshchenko, T.; Jiang, G.; Kondratenko, V. A.; Rodemerck, U.; Kondratenko, E. V., Current status and perspectives in oxidative, non-oxidative and CO2-mediated dehydrogenation of propane and isobutane over metal oxide catalysts. *Chem. Soc. Rev.* **2021**, *50*, 473-527.
- (78) Docherty, S. R.; Rochlitz, L.; Payard, P.-A.; Coperet, C., Heterogeneous alkane dehydrogenation catalysts investigated via a surface organometallic chemistry approach. *Chem. Soc. Rev.* **2021**, *50*, 5806-5822.
- (79) Han, S.; Zhao, D.; Otroshchenko, T.; Lund, H.; Bentrup, U.; Kondratenko, V. A.; Rockstroh, N.; Bartling, S.; Doronkin, D. E.; Grunwaldt, J.-D., Elucidating the Nature of Active Sites and Fundamentals for their Creation in Zn-Containing ZrO₂–Based Catalysts for Nonoxidative Propane Dehydrogenation. *ACS catal.* **2020**, *10*, 8933-8949.
- (80) Hu, B.; Schweitzer, N. M.; Zhang, G.; Kraft, S. J.; Childers, D. J.; Lanci, M. P.; Miller, J. T.; Hock, A. S., Isolated FeII on silica as a selective propane dehydrogenation catalyst. *ACS catal.* **2015**, *5*, 3494-3503.
- (81) Zhang, H.; Liu, G.; Shi, L.; Ye, J., Single-Atom Catalysts: Emerging Multifunctional Materials in Heterogeneous Catalysis. *Advanced Energy Materials* **2018**, 8.
- (82) Yang, X. F.; Wang, A.; Qiao, B.; Li, J.; Liu, J.; Zhang, T., Single-Atom Catalysts: A New Frontier in Heterogeneous Catalysis. *Acc. Chem. Res.* **2013**, *46*, 1740.

- (83) Sharma, P.; Kumar, S.; Tomanec, O.; Petr, M.; Zhu Chen, J.; Miller, J. T.; Varma, R. S.; Gawande, M. B.; Zboril, R., Carbon Nitride-Based Ruthenium Single Atom Photocatalyst for CO2 Reduction to Methanol. *Small* **2021**, *17*.
- (84) Kadam, R. G.; Zhang, T.; Zaoralova, D.; Medved, M.; Bakandritsos, A.; Tomanec, O.; Petr, M.; Chen, J. Z.; Miller, J. T.; Otyepka, M.; Zboril, R.; Asefa, T.; Gawande, M. B., Single Co-Atoms as Electrocatalysts for Efficient Hydrazine Oxidation Reaction. *Small* **2021**, *17*.
- (85) Marshall-Roth, T.; Libretto, N. J.; Wrobel, A. T.; Anderton, K.; Surendranath, Y., A Pyridinic Fe-N4 Macrocycle Effectively Models the Active Sites in Fe/N-Doped Carbon Electrocatalysts. **2019**.

Graphical Abstract



Formation of PtP₂ leads to isolated Pt²⁺ sites and a large decrease in the energy of the filled Pt 5d orbitals, leading to different catalytic properties from metallic Pt NPs.